Available online at www.sciencedirect.com

ScienceDirect

Underground Space 26 (2026) 479–497

www.keaipublishing.com/undsp

Research Paper

Degradation mechanism of microstructure of residual coal pillars during highly mineralized mine-water storage in coal mine goaf

Hao Liu [a], Zenghui Zhao [a,b,*], Qing Ma [c,d], Xiaoli Liu [d], Longjie Zhu [a]

[a] College of Energy and Mining Engineering, Shandong University of Science and Technology, Qingdao 266590, China
[b] State Key Laboratory of Disaster Prevention and Ecological Protection in Open-pit Coal Mines, Shandong University of Science and Technology, Qingdao 266590, China
[c] Beijing Key Laboratory of Urban Underground Space Engineering, University of Science and Technology Beijing, Beijing 100083, China
[d] State Key Laboratory of Hydroscience and Engineering, Tsinghua University, Beijing 100084, China

Received 20 May 2025; received in revised form 18 October 2025; accepted 28 October 2025
Available online 24 December 2025

Abstract

Driven by the "dual carbon" strategy, the functionality of coal mine underground reservoirs is transitioning toward multimedia collaborative storage, such as CO_2 geological sequestration and strategic energy reserves. The microscopic structures of the coal pillar dams, which are subjected to mining-induced damage and long-term infiltration erosion by highly mineralized mine water, continuously deteriorate over time, posing significant risks to the long-term safety and stability of the reservoirs. This study, based on the Lingxin Coal Mine Underground Reservoir Demonstration Project, employs a multi-technique characterization approach including X-ray diffraction (XRD), scanning electron microscope, nuclear magnetic resonance, and computed tomography to systematically reveal the multiscale collaborative erosion mechanisms of highly mineralized mine water on the mineral composition, crystal structure, and pore development of coal pillar dams. The results indicate: (1) significant concentration-dependent deterioration of mineral composition and crystal structure; kaolinite hydrolysis had a weakening effect on XRD peaks while quartz remained inert; (2) initiation of progressive microstructural damage at boundaries via dissolution/loosening; this damage advanced through layered mineral delamination and pore development (evidenced by NMR T_2 broadening), resulting in irreversible void formation with chloride precipitation; (3) formation of pore-throat halite crystals, primarily due to chloride ions (Cl^-); these crystals propagated microfractures through salt-expansion stress, establishing a cyclic dissolution–migration–crystallization–cracking process; (4) triggering of accelerated deterioration of the coal matrix owing to prolonged retention; this induced time- and concentration-dependent expansion and interconnection of pore-fracture networks, resulting in geomechanical deterioration.

Keywords: Highly mineralized mine water; Underground storage; Coal pillar dam; Microstructure; Degradation mechanism

1 Introduction

The northwestern region of China (Shanxi, Shaanxi, Inner Mongolia, Gansu, and Ningxia), as the national energy strategic core area, possesses resource advantages of shallow burial depth (<500 m) and excellent coal quality (ash content <15%), contributing to more than 50% of China's total coal production capacity (Xie et al., 2018; Ai et al., 2021; Zhang et al., 2021; Chen et al., 2023). However, the inherent water scarcity of the region, with annual average precipitation below 400 mm (Zhou et al., 2023; Pan et al., 2023), conflicts sharply (Fig. 1) with its high-intensity mining activities (recovery rate >80%). This contradiction triggers a chain reaction of ecological degradation: mining-induced fractures connected with aquifers cause groundwater leakage rates of 60%–80% (Fang et al., 2022; Dai et al., 2025), leading to severe surface

* Corresponding author at: College of Energy and Mining Engineering, Shandong University of Science and Technology, Qingdao 266590, China.
E-mail address: skd992945@sdust.edu.cn (Z. Zhao).
Peer review under the responsibility of Tongji University

https://doi.org/10.1016/j.undsp.2025.10.001

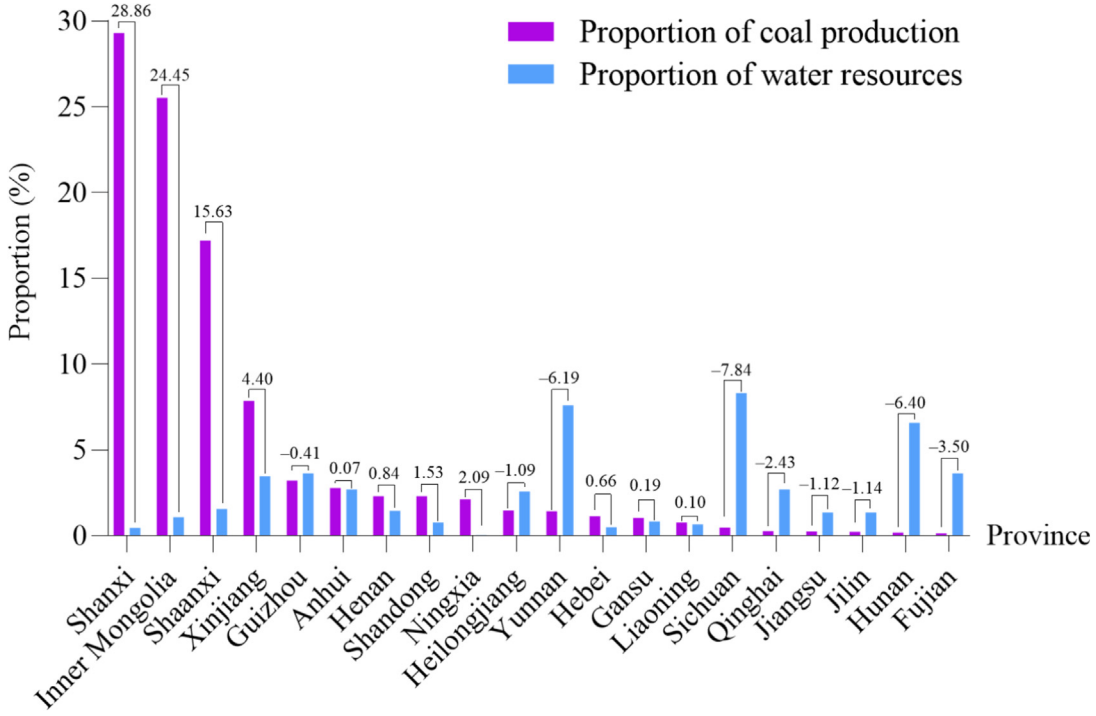

Fig. 1. Percentage of coal production and water resources in each province in 2024 (Source: Annual report of China Coal Industry Association).

subsidence (>200 mm/a) and vegetation coverage decline (Gu et al., 2015; Xu et al., 2023; Wu et al., 2023). These environmental challenges have significantly constrained the sustainable development of mining areas.

To address such resource–environment coordination challenges, the Shenhua Group pioneered an integrated technical system of "diversion–storage–utilization" for mine water management (Gu et al., 2015; Fang et al., 2022). This innovation leverages the self-sealing effect of coal or rock masses in goaf areas (permeability coefficient $<10^{-7}$ cm/s) and safety coal pillars (width-to-height ratio >2.0) to construct clustered underground coal mine reservoirs (Fig. 2). Engineering practices (Shen et al., 2020; Chu et al., 2024; Xu et al., 2025) demonstrate that this technology achieves 95% recycling efficiency of mine water, with single-reservoir storage capacity reaching 3×10^6 m^3. This effectively alleviates the conflict between safe, efficient, and green coal mining and water resource conservation/utilization in the western mining regions.

With the promotion of the "dual carbon" strategy, underground coal mine reservoirs are undergoing functional transformation—expanding from water resource storage to multimedia sequestration scenarios such as CO_2 storage (sequestration potential >30 Mt/a) and strategic energy reserves (Liu et al., 2019; Chen et al., 2022). In this process, dam stability faces dual challenges. First, the dam structure exhibits substantial geological defects. Owing to primary fracture development (fracture density >5 cracks/m) and anisotropic strength characteristics (strength variation coefficient >0.35) (Cui et al., 2020; Craig et al., 2021; Berrezueta et al., 2023; Huang et al., 2024), residual coal pillars in goaf areas undergo accelerated damage accumulation under the coupled static–dynamic loads of dynamically evolving mining-induced stress fields (vertical stress fluctuation amplitude >8 MPa) and dynamic disturbances from overlying rock fractures (energy release $>10^3$ J) (Li et al., 2017; Zhang et al., 2024c). Second, the highly mineralized mine water in northwestern regions (total dissolved solid (TDS) >10 g/L, with Cl^- and SO_4^{2-} accounting for >40%) (Zhao et al., 2023; He et al., 2024; Saberi & Vriens, 2025) induces multiscale structural degradation of coal-rock through long-term chemical–mechanical coupling effects, including ion migration–crystallization pressure (pressure gradient >1 MPa/m) and mineral dissolution–reorganization (solubility >20%) (Pazki et al., 2025; Zhao et al., 2025). This degradation manifests as microscale pore topology reconstruction, mesoscale fracture network percolation evolution, and macroscale bearing strength attenuation, which collectively pose considerable challenges to the long-term safety of reservoir sequestration (Tang et al., 2023; Zeng et al., 2024; Khimulia et al., 2024; Fang et al., 2024; Li et al., 2024; Kong et al., 2024).

Existing research has predominantly focused on the macroscopic stability analysis of reservoirs; studies on the cross-scale damage and deterioration mechanisms of coal rock under the coupled effects of highly mineralized environments, multiphase media, and mechanical loads have been limited. To address this, this study conducted multiscale micro–nanostructural observation experiments at the Lingxin Coal Mine Underground Reservoir. This research revealed the micro–nanostructural deterioration

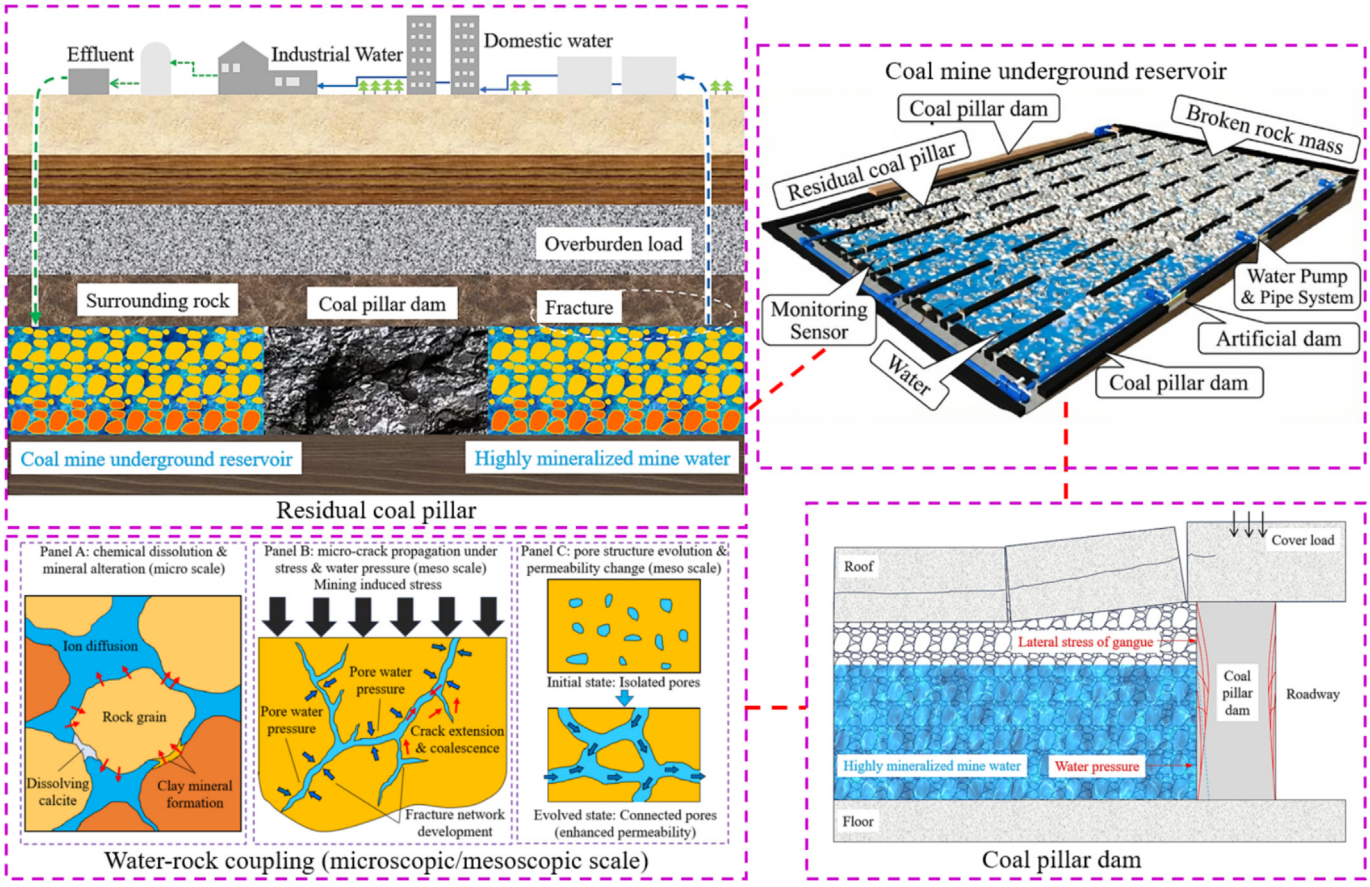

Fig. 2. Bearing structure of underground water reservoirs in mine and schematic of rock deterioration due to water (Zhang et al., 2021; reproduced with permission, courtesy of Elsevier).

mechanisms of coal rock under highly mineralized mine water erosion. An equivalent pore network model of coal rock under hydro–mechanical–chemical (HMC) coupling was established to elucidate the time-dependent percolation characteristics of fracture networks in concentrated brine reservoir coal pillar dam structures. These findings provide theoretical support for life-cycle safety control of coal mine underground reservoirs and possess substantial engineering value for advancing the green transformation of coal resource development and underground space utilization.

2 Experimental

2.1 Coal pillar sample preparation

Coal specimens were sourced from Panel 12,306 of the Lingxin Coal Mine Underground Reservoir Demonstration Project in the Ningdong Coalfield, Ningxia (L1614 and L1814 gate roads). As shown in Fig. 3, the sampling area is a low-rank anthracite seam with gangue interlayers, exhibiting well-developed natural fracture systems. To minimize heterogeneity impacts, intact primary coal blocks were selected, transported to the laboratory under plastic film encapsulation, and processed into Φ50 mm × 100 mm cylindrical specimens per ISRM standards. Both end surfaces were precision-ground (flatness <0.01 mm), complying with Methods for determining the physical and mechanical properties of coal and rock—Part 1: General requirements for sampling (GB/T 23561.1—2024). The specimens in each test group originated from identical stratigraphic horizons. Concurrently, Φ10 mm × 20 mm micro-cylindrical specimens (surface roughness ≤0.8 μm) were prepared for scanning electron microscope (SEM), X-ray diffraction (XRD), nuclear magnetic resonance (NMR), and computed tomography (CT) characterization. Standard specimens exhibiting P-wave velocities of 2100–2300 m/s were selected for the highly mineralized mine water erosion experiments.

2.2 Preparation of highly mineralized mine water erosion solution

Highly mineralized mine water samples collected from the Lingxin Coal Mine site were sent to a third-party water quality testing and analysis institution for detailed chemical composition analysis. Both the collected water samples and those used during the experiments were tested in accordance with national environmental protection standards (Berrezueta et al., 2023). Each water quality parameter was tested at least three times in replicate, and the average

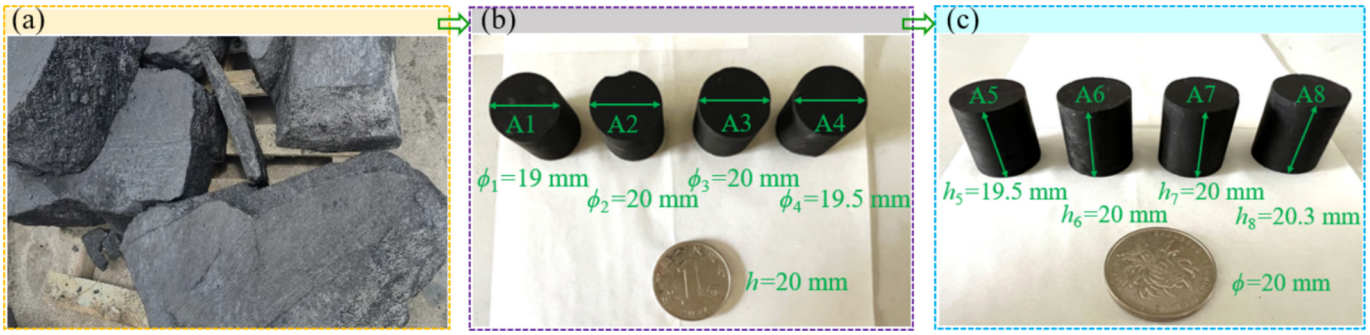

Fig. 3. Samples from Lingxin Coal Mine and their preparation. (a) Coal blocks sampled on site, (b) micro coal sample diameter, and (c) micro coal sample height.

values were calculated for subsequent analyses. The sealed, highly mineralized mine water primarily contained K^+, Ca^{2+}, Na^+, Mg^{2+}, Cl^-, SO_4^{2-}, and HCO_3^-. The average ion concentrations obtained from the quality analyses of water samples collected from multiple locations are summarized in Table 1. The average pH of the solution was 7.48, indicating a weakly alkaline nature.

The concentration gradients (1C: 36 000 mg/L; 0.5C: 18 000 mg/L; 0.1C: 3600 mg/L) were designed based on the baseline maximum mineralization level obtained from in situ mine water monitoring, corresponding to the key environmental evolution stages during water-conducting fracture development in a mining-disturbed overburden. The 1C concentration simulates the high-mineralization upper-limit condition of the pristine confined reservoir stage; 0.5C represents the moderate-mineralization infiltration state induced by localized fracture development involving water–rock interactions and gravity-driven seepage; 0.1C reflects the low-mineralization diluted seepage following fracture network connectivity with the aquifer. Accordingly, the comprehensive "high-mineralization erosion (1C)–moderate-mineralization immersion (0.5C)–low-mineralization migration (0.1C)" experimental simulation framework was established to systematically reveal the nonlinear evolution characteristics of solution concentration effects on coal rock HMC coupling damage. The findings provide quantitative experimental evidence to elucidate multifield coupling mechanisms of reservoir degradation during geological storage. The formulation scheme for the highly mineralized solutions based on the water-quality analysis results is presented in Table 2.

Table 1
Average ion concentrations in highly mineralized mine water samples of underground reservoir in Lingxin Coal Mine.

Items	Unit	Results
No.	–	LX23-12
pH	–	7.48
K^+	mg/L	50.5
Na^+	mg/L	8116.24
Ca^{2+}	mg/L	774
Mg^{2+}	mg/L	605
NH_4^+	mg/L	–
Ammonia nitrogen	mg/L	–
Chemical oxygen demand	mg/L	380.98
Total carbon	mg/L	284.6
Total organic carbon	mg/L	8.32
Electric conductivity	mS/cm	22.5
Cl^-	mg/L	9881.7
SO_4^{2-}	mg/L	6216.4
NO_3^-	mg/L	–
$S_2O_3^{2-}$	mg/L	–
HCO_3^-	mg/L	2162
CO_3^{2-}	mg/L	172
Turbidity	–	0.5
Chromaticity	–	50

Highly mineralized aqueous solutions were prepared using the ionic equivalent ratio method. Analytical-grade potassium sulfate, sodium sulfate, calcium chloride, sodium carbonate, sodium chloride, and sodium bicarbonate were selected as the primary ion sources, and their mass fraction ratios were strictly based on mine water ion chromatography data. Through a three-step chemical gradient design (mineralization gradients: 3600, 18 000, and 36 000 mg/L), a highly mineralized mine water sequestration simulation system was established to cover the entire lifecycle (0–4 a) of underground reservoirs. The detailed solution preparation procedure is illustrated in Fig. 4.

To eliminate the influence of compositional fluctuations in the original mine water (e.g., ion concentrations and suspended solids) on the experimental results, the following procedure was implemented based on the experimental design. First, the 1C concentration standard solution was prepared by precisely weighing corresponding compounds (weighing error ≤0.01 g). After weighing, analytical-grade compounds were sequentially added to a clean beaker, and the volume of distilled water was calculated. The mixture was stirred thoroughly using a glass rod to ensure complete dissolution. After stirring, insoluble impurities and suspended particles in the solution were removed via filtration through a double-layered qualitative filter paper to obtain a 1C concentration standard solution. This solution was then used as a stock solution to prepare 0.5C and 0.1C concentration solutions via proportional dilution. This method, which incorporates compositional calibration and standardized operations, ensures gradient consistency

Table 2
Highly mineralized mine water solution ratio scheme.

Highly mineralized mine water solution		
Solute		Solvent
Chemical composition	Precise mass (g/L)	
K_2SO_4	0.11	Deionized water
$CaCl_2$	2.15	
$MgSO_4$	3.03	pH regulator
NaCl	14.02	HCl (Alternate selection)
Na_2SO_4	5.61	NaOH (Alternate selection)
$NaHCO_3$	2.98	pH
Na_2CO_3	0.31	7.48

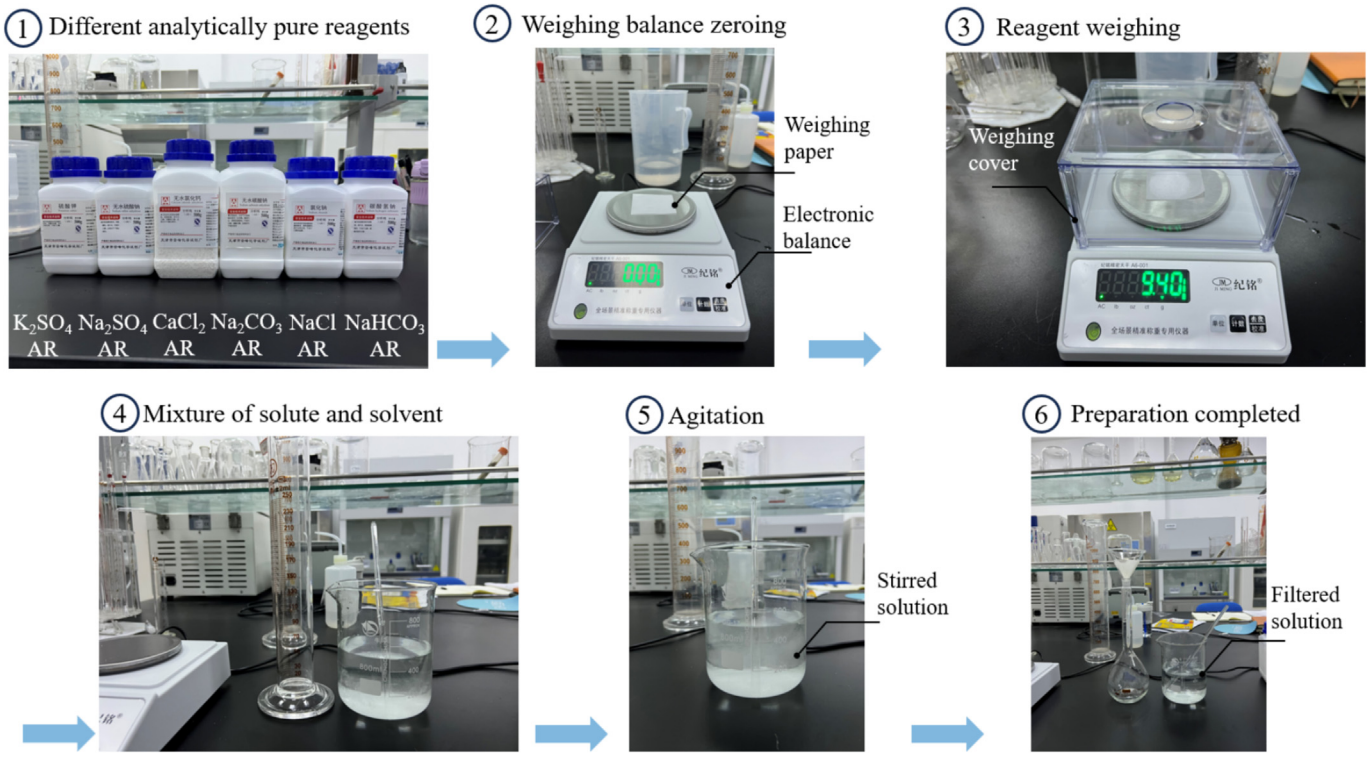

Fig. 4. Highly mineralized mine water solution configuration process.

across concentration groups and guarantees experimental reproducibility.

2.3 Design and operation process of long-term seepage immersion device

A coal pillar dam is subjected to long-term exposure to a complex coupled HMC field environment involving multi-physical field interactions, such as confining pressure, hydrochemical conditions, and temperature fields. To accurately simulate this complex environment, experiments were conducted using an in-house-developed coal or rock pressurized permeation soaking experimental system, as illustrated in Fig. 5. The experimental apparatus consisted of four core modules: a pressurized permeation chamber, servo-controlled hydraulic circulation system, sealed pressure control system, and digital control system. It enables precise control of critical parameters, including the confining pressure (0–5 MPa), permeation rate (0–10 mL/min), and hydrochemical conditions (pH 2–12), thereby achieving multiscale and multifield coupled simulations that replicate the actual environmental conditions experienced by coal pillar dams in underground mine reservoirs.

The pressurized permeation chamber was constructed from cylindrical 316L stainless steel and featured multiple size specifications (internal diameter × outside diameter: 100 mm × 120 mm, 180 mm × 200 mm, and 250 mm × 300 mm) to accommodate diverse experimental requirements. The pressure head incorporated a grid-patterned groove on its top surface to ensure uniform liq-

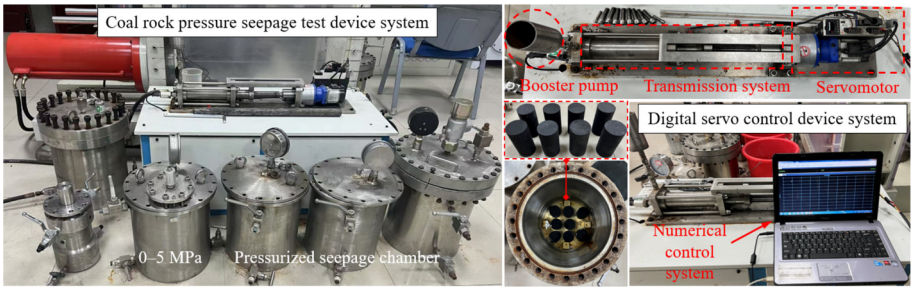

Fig. 5. Testing equipment and its parts.

uid permeation, whereas lateral grooves were distributed along its sidewalls to secure the O-rings for enhanced sealing performance. Both the top of the chamber and the upper platen were sealed with rubber rings to effectively prevent pressurized water leakage during operation.

The servo-pressurized water circulation and numerical control system comprises three principal components: a servomotor, digital controller, and hydraulic circulation system. Using gas-driven water injection technology, this system injects and maintains solutions of varying concentrations in continuous circulation, thereby ensuring a uniform fluid flow through the test specimens. The operational software, hosted on a central computer, programmed the filling and pressurization commands that were transmitted to the digital servo controller. This controller actuates the servomotor, which drives the booster pump piston via mechanical transmission, thereby achieving precise filling and pressure application in the permeation chamber. Real-time pressure monitoring is accomplished using integrated pressure sensors that feed the data back into the acquisition system. Upon reaching preset hydraulic pressure thresholds, the system automatically issued termination commands while maintaining a stable pressure through servo-motor modulation, establishing a closed-loop control mechanism compliant with ISO 1219-1 fluid power standards.

The sealed pressure system consisted of a pressure cylinder and gas cylinders designed to apply confining pressure conditions. During the experiments, the pressure of the gas cylinder was regulated to ensure that the confining pressure consistently exceeded the permeation pressure of the water circulation system. This establishes an equilibrium between the permeation and confining pressures, effectively preventing lateral solution migration while maintaining uniformity and stability during the soaking process. The closed-loop pressure-control mechanism guarantees experimental repeatability under precisely maintained boundary conditions.

Pre-test treatment: Coal samples were placed in a vacuum chamber and evacuated to an absolute pressure below 10^{-3} Pa to ensure the complete evacuation of internal pores. Subsequently, the samples were statically incubated for 8 h to stabilize the vacuum state. Following this, a pre-prepared, highly mineralized aqueous solution was injected to fully submerge the coal specimens, guaranteeing uniform saturation under controlled hydrochemical conditions.

Experimental procedure: All system components, including the confining pressure system, hydraulic circulation system, and data acquisition modules, were connected in accordance with standard operating procedures. The pretreated coal sample was positioned in a high-pressure permeation chamber, and a confining pressure system was initiated to establish preset confining pressure conditions. Based on breakthrough pressure test results, the hydraulic system pressure parameters were configured while regulating the gas-cylinder pressure to maintain a confining pressure that exceeded the hydraulic pressure. This resulted in a constant-rate fluid migration through the specimen (flow rate: 0.5–1.0 mL/min). To eliminate photochemical interference, the entire immersion assembly was operated within a light-proof enclosure compliant with ASTM G154-16 cyclic weathering testing standards.

To establish equivalent mapping between short-term experimental observations and long-term engineering behaviors through a concentration-driven enhancement mechanism in chemical field dynamics, the mineral dissolution rate (R) and solution ion activity (a_i) are governed by the following relationship based on the Eyring–Polanyi transition state theory:

$$R = k_0 \cdot \exp\left(-\frac{E_a}{R_{gas}T}\right) \cdot \prod a_i^{m_i}, \tag{1}$$

where E_a denotes the reaction activation energy, and m_i represents the reaction order of each ion, R_{gas} represents the general gas constant (8.314 J·mol^{-1}·K^{-1}), and i is the subscript index, representing different ionic components. k_0 denotes the rate constant in the standard state, and T denotes the absolute temperature (K). In highly mineralized mine water solutions (1.0C, 36 000 mg/L), the activities of Na^+ and Cl^- exhibit a 152-fold increase compared to that in 0.1C solutions (verified from ion-selective electrode measurements), resulting in a 15.4kJ/mol reduction in kaolinite dissolution activation energy.

This establishes the concentration–time equivalence factor η:

$$\eta(C_1, C_3) = \left(\frac{C_1}{C_3}\right)^m \cdot \exp\left[\frac{E_a(C_1) - E_a(C_3)}{RT}\right], \tag{2}$$

where C_1 and C_3 are the engineering concentrations corresponding to the experimental concentrations of 3600 mg/L and 36 000 mg/L, respectively. $C_3 = 3600$ mg/L serves as the engineering reference concentration, with calibrated parameters $m = 1.32$ (determined via batch reactor titration) and $E_a(C_1) - E_a(C_3) = 15.4$ kJ/mol. When $C_1 = 36\,000$ mg/L (1.0C), the equivalence factor yields $\eta = 34.6$. Calculations demonstrate that 80 days of chemical erosion under 1.0C solution immersion equivalently corresponds to $80 \times 34.6 = 2768$ d (7.6 a) under 0.1C solution exposure. Based on the revised multi-ion activity and equivalence factor models combined with the experimentally set concentration and time gradients, the equivalence relationship between each combination, and the engineering baseline time was calculated, as presented in Table 3.

The test was designed with immersion time gradients of 0, 5, 10, 15, 20, 40, 60, 80, and 100 d, covering three phases of hydro–mechanical–chemical–thermal synergistic effects: initial permeation ($T \leq 10$ d), accelerated phase transition (10 d $< T \leq 60$ d), and stabilized damage ($T > 60$ d). During the test, the confining pressure, osmotic pressure, and flow rate were monitored in real time with a data acquisition frequency of 1 Hz to ensure a precise capture of the time-varying responses.

Post-test processing: After immersion, the coal samples were removed, the surface moisture was wiped off using an absorbent paper, and the samples were wrapped in a plastic film to isolate them from oxygen and moisture in the air, effectively preventing the effects of weathering on their physicochemical properties. The wrapped coal samples were then transferred to the subsequent testing phases for physical and mechanical property testing and microstructural analyses.

Highly mineralized mine water erosion experiments and breakthrough pressure tests served as preconditioning experiments, providing essential prerequisites for subsequent micro–nanoscale observation experiments, uniaxial compression experiments, and analyses, as shown in Fig. 6.

All specimens were labeled using a numbering system (concentration–immersion age–sequence number), and their initial morphological characteristics were documented using high-resolution camera photography. Precise electronic analytical balances were used to weigh the specimens before and after immersion, providing the initial state parameters for subsequent multiscale mechanical response analysis.

Based on the low permeability ($K < 0.1$ mD) and non-Darcy seepage characteristics of anthracite, coal samples 3 and 4 were selected for breakthrough pressure testing before injecting the solution. Porosity and permeability tests were first conducted on the coal samples according to the standard requirements. The measured porosity values for the three groups of coal samples were 3.26%, 5.53%, and 6.64%, with permeabilities of 4.29×10^{-3}, 10.21×10^{-3}, and 13.72×10^{-3} mD, respectively. After vacuuming, the coal samples were saturated with highly mineralized mine water under a pressure of 1 MPa for 24 h and then placed in a core holder with a net confining pressure of 1.44 MPa. Starting from the initial pressure difference, the pressure was increased by 0.2 MPa every 30 min while monitoring bubble emergence at the outlet. Test results showed breakthrough pressures of 0.6 MPa for coal samples 1 and 2, and 0.42 MPa for coal sample 3, yielding average breakthrough pressure of 0.56 MPa. Based on these results, the maximum breakthrough pressure (0.60 MPa) was selected as the inlet pressure for the coal rock in subsequent experiments.

3 Results and analysis

3.1 Age erosion effect of highly mineralized mine water on mineral phase and diffraction characteristics of coal sample

Figures 7 and 8 present the XRD patterns of coal samples in their natural state and those immersed under highly mineralized mine water for different durations. The initial coal samples primarily consist of mineral components such as quartz (SiO_2), calcite ($CaCO_3$), kaolinite ($Al_2Si_2O_5(OH)_4$), albite ($NaAlSi_3O_8$), and orthoclase ($KAlSi_3O_8$).

By comparing the XRD patterns of the sample in the natural state (N0–0 d) with those of samples under different immersion ages, it was observed that the peak intensities of the overall diffraction spectra remained relatively stable. However, the distinct kaolinite peaks under natural conditions significantly decreased after exposure to highly mineralized mine water. This phenomenon indicates that

Table 3
Equivalent relationship between each combination and the engineering reference time.

Test duration (d)	Equivalent engineering time					
	Concentration #1 (36 000 mg/L)		Concentration #2(18 000 mg/L)		Concentration #3 (3600 mg/L)	
5	173.0 d	0.5 a	67.5 d	0.2 a	5.0 d	0.0 a
10	346.0 d	0.9 a	135.0 d	0.4 a	10.0 d	0.0 a
15	519.0 d	1.4 a	202.5 d	0.6 a	15.0 d	0.0 a
20	692.0 d	1.9 a	270.0 d	0.7 a	20.0 d	0.1 a
40	1384.0 d	3.8 a	540.0 d	1.5 a	40.0 d	0.1 a
60	2076.0 d	5.7 a	810.0 d	2.2 a	60.0 d	0.2 a
80	2768.0 d	7.6 a	1080.0 d	3.0 a	80.0 d	0.2 a
100	3460.0 d	9.5 a	1350.0 d	3.7 a	100.0 d	0.3 a

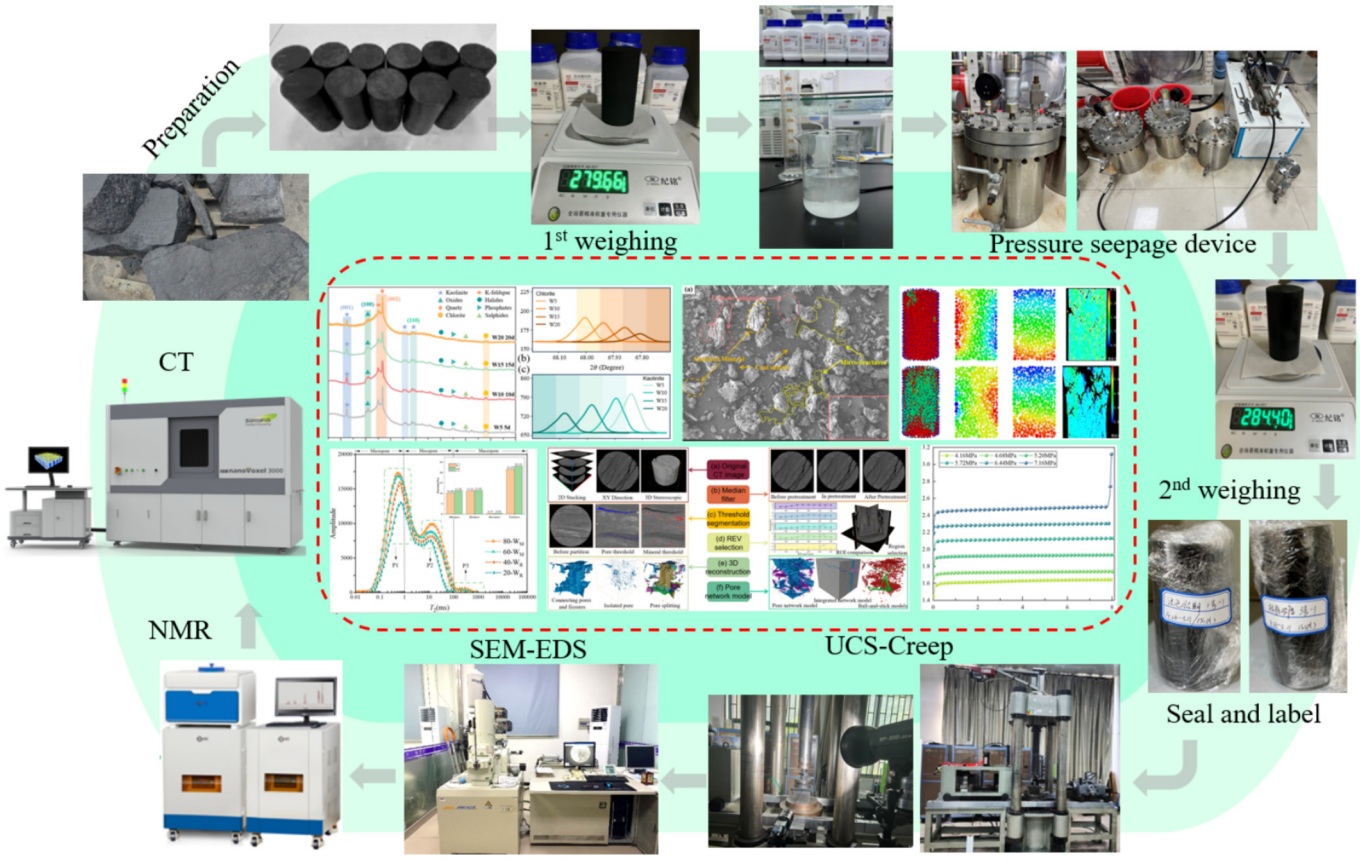

Fig. 6. Immersion erosion test process.

prolonged immersion leads to corrosion, dissolution, or chemical reactions between the highly mineralized mine water and the minerals in the coal. Specifically, kaolinite was still detectable in the coal samples after 5 and 10 d of interaction with the highly mineralized mine water. However, when the immersion age was extended to 15 and 20 d, the diffraction peaks of kaolinite were markedly weakened, showing only minor and low-intensity peaks. This suggests that kaolinite, as a layered silicate mineral, undergoes structural changes in highly mineralized mine water, gradually dissolving or transforming into other mineral forms during prolonged immersion.

Notably, quartz exhibits extremely high physical and chemical stability, enabling its crystal structure to remain intact without substantial changes under the erosive effects of highly mineralized mine water. XRD pattern analysis further corroborated this characteristic, as the diffraction peak positions and quantities of quartz demonstrated consistent stability regardless of the immersion duration. However, with prolonged immersion, despite the persistent stability of the quartz crystal structure, changes in its surrounding environment, particularly significant alterations in other minerals or organic components, may indirectly influence the diffraction peaks of quartz.

The strongest and sharpest diffraction peak observed at 26.58° corresponded to the characteristic quartz (1 0 1) peak. This intense peak indicates high quartz content in the coal sample and a well-developed crystal structure. The height and sharpness of the (1 0 1) peak reflect a high degree of ordering in the quartz crystals, suggesting a favorable orientation of the aromatic lamellae in the coal sample. The prominent diffraction peak appearing at 12.21° represents the most distinctive (0 0 1) peak of kaolinite, generated by the reflection from the (0 0 1) crystal plane in its layered structure. This typical (0 0 1) peak indicates a relatively high kaolinite content in the coal sample and good crystallinity. However, compared to the characteristic quartz peaks, the (0 0 1) peak of kaolinite exhibited a lower height and broader sharpness, indicating smaller grain sizes or the presence of microscopic defects in the kaolinite crystals.

With prolonged immersion age, the interlayer spacing d_{002} in the coal samples gradually increased, whereas the degree of aromatization f_a decreased. This phenomenon indicates that corrosive ions such as chloride salts in highly mineralized mine water infiltrated the aromatic lamellae of coal and disrupted its aromatic layer structure. This led to an increase in the interlayer spacing

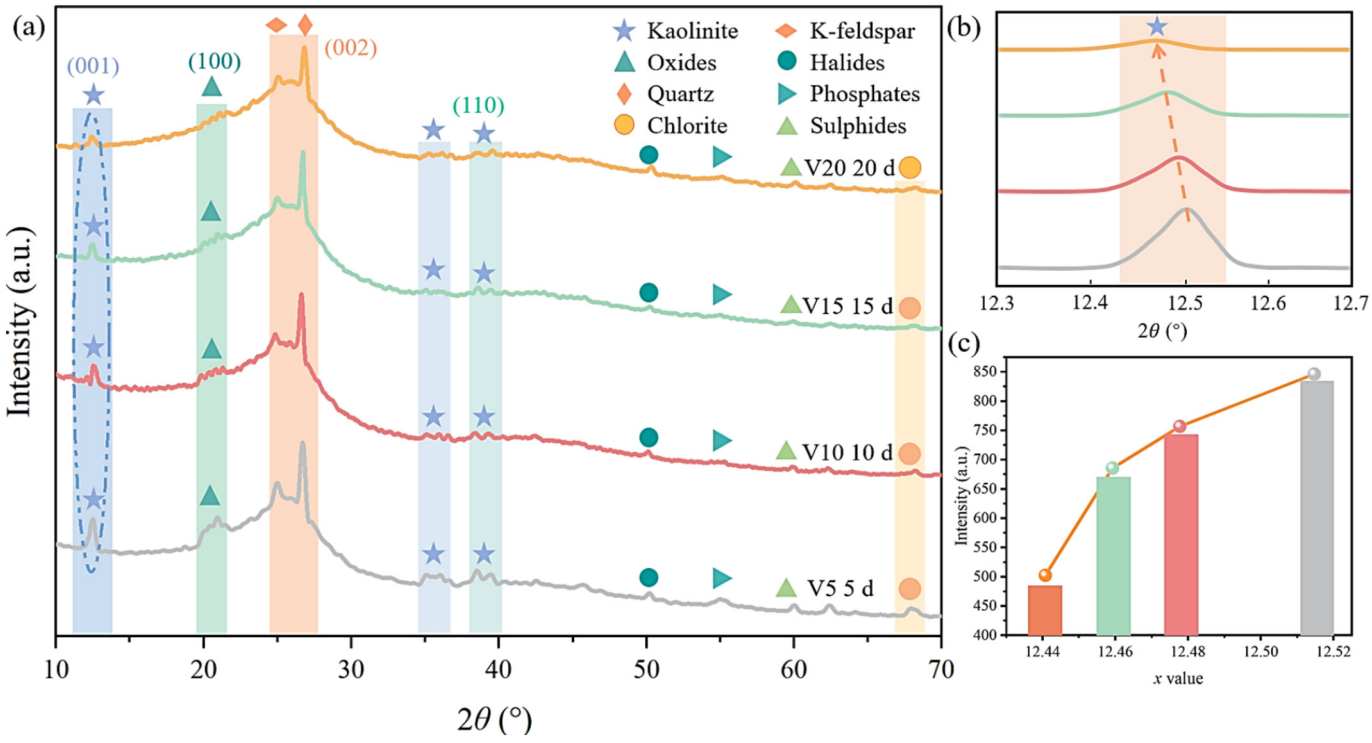

Fig. 7. XRD spectra of coal samples with different immersion periods (V5–V20 groups) under 0.5C concentration.

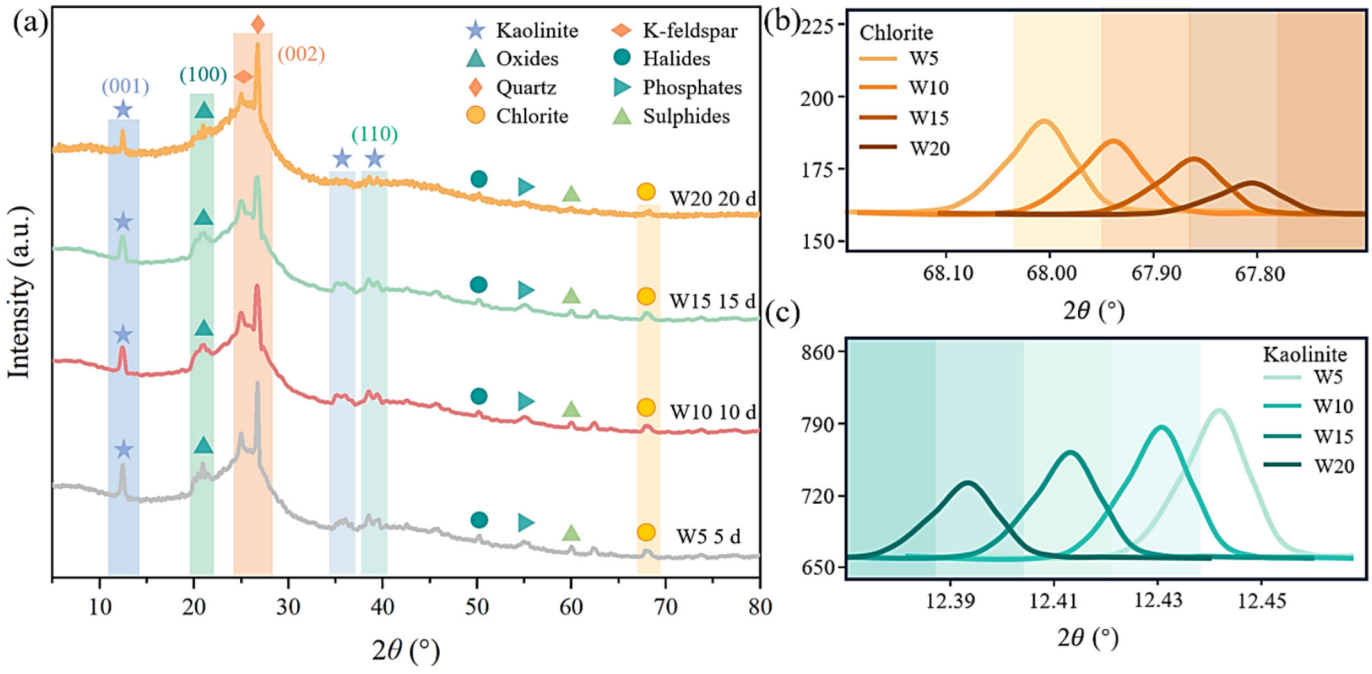

Fig. 8. XRD spectra of coal samples with different immersion periods (W5–W20 groups) under 0.1C concentration.

and rendered the aromatic structure of the coal more disordered or fragmented. Additionally, the stacking height L_c and average diameter L_a of the aromatic lamellae progressively diminished. This suggests that erosion from highly mineralized mine water not only weakens the connections between the lamellae but also corrodes their edges, resulting in further reductions in their dimensions.

3.2 Age gradient erosion effect of highly mineralized mine water on micro-morphological characteristics of coal sample

Figure 9 presents the evolution of surface morphology in anthracite coal samples under highly mineralized mine water erosion at different immersion ages. As a typical anthracite (or lean coal, graphite coal), the coal samples exhibit a distinct layered microstructure, which displays a highly ordered arrangement under high-magnification observation. The coal matrix features a dense structure with low porosity, and the microscopic surface is almost entirely covered by organic matter. By comparing the micromorphology of coal samples across immersion ages, a clear trend of structural changes can be observed: in the natural state, mineral particles exhibit sharp boundaries and well-defined edges; during the initial erosion stage, changes are concentrated at the boundaries, starting from microscopic edges and gradually spreading across the sample. As the immersion age increases, the boundaries gradually become blurred, developing flocculent structures and layered exfoliation. In later erosion stages, chemical infiltration penetrates all structural levels of the coal sample, leading to an irreversible damage phase in its microstructure. This progression visually illustrates the gradual impact of highly mineralized mine water on the micromorphology of the coal samples.

This progressive evolution of the micromorphology results from the synergistic effects of multiple factors, revealing the physicochemical behavior of coal pillar dams in long-term, highly mineralized mine water environments (Zhang et al., 2024a, 2024b). First, the ionic components in the highly mineralized mine water gradually dissolved certain minerals in the coal sample, leading to the gradual disappearance of mineral particle boundaries. This dissolution not only altered the morphology of the mineral particles, but also affected the overall physical properties of the coal samples. Second, as erosion progressed, the dissolved mineral particles migrated and were redeposited on the coal surface, forming flocculent structures. This process enhanced the surface coverage layer, thereby influencing

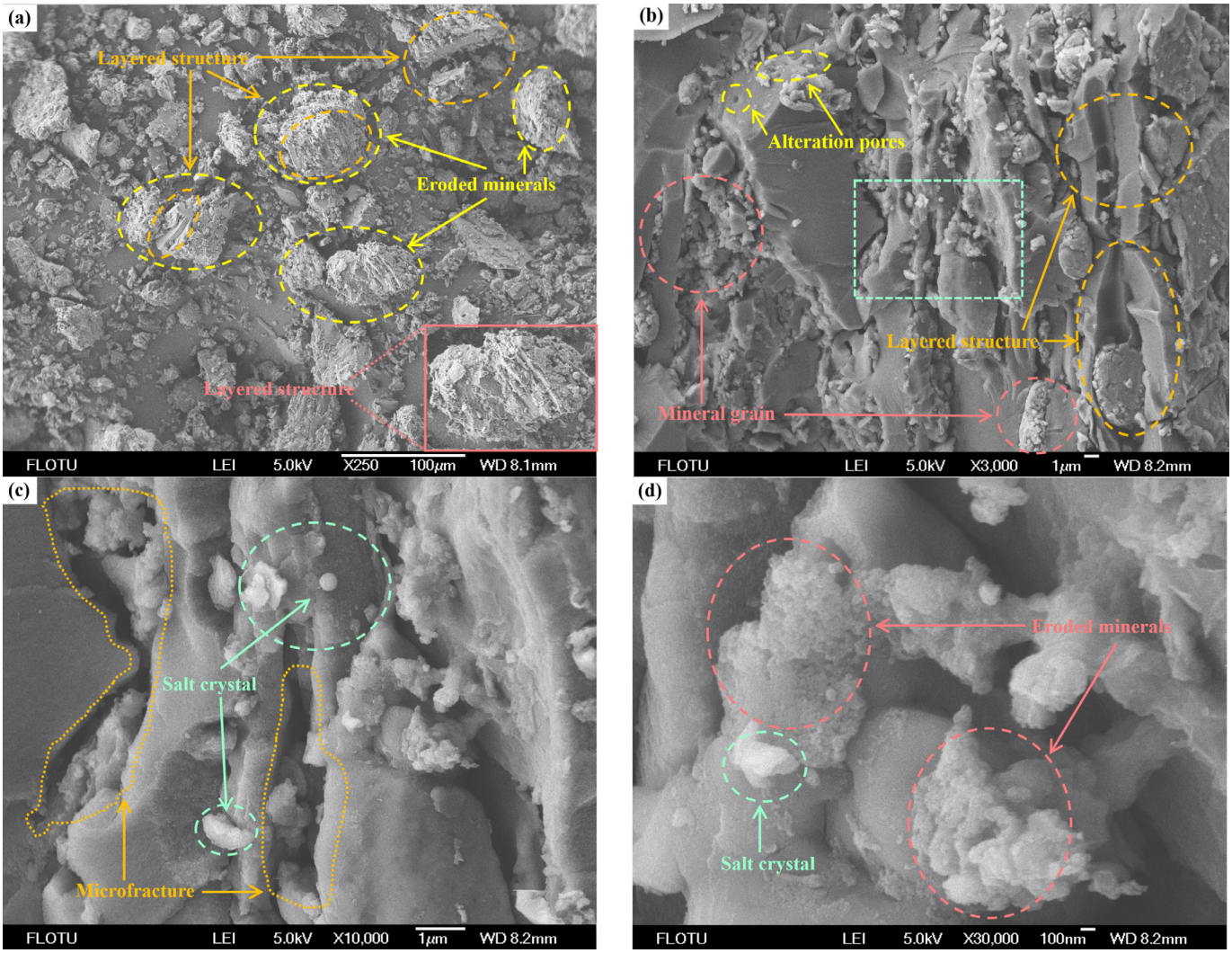

Fig. 9. M-30: Soaking age = 30 d (late stage erosion).

the gas and water permeabilities of the coal sample. Additionally, chemical reactions occur between the components in the solution and the organic matter or minerals in the coal, generating new mineral phases. These newly formed mineral phases fill the existing pores, rendering the coal surface more compact and reshaping the morphology of the mineral particles.

3.3 Pore structure and nuclear magnetic resonance characteristics of eroded coal sample

In the study of porous coal samples, NMR technology has been used to analyze pore types and sizes. Different pore types (micropores, mesopores, and macropores) exhibit distinct characteristic peaks in the NMR spectra. By analyzing the positions, intensities, and shapes of these characteristic peaks, critical information such as the pore type, size distribution, and connectivity can be revealed. NMR technology primarily utilizes the nuclear magnetic resonance effect of hydrogen nuclei (^{1}H), as coal rock pores contain water or other hydrogen-bearing fluids. A Carr–Purcell–Meiboom–Gill (CPMG) sequence was employed to obtain the relaxation times and initial magnetization vectors of the pores, and the transverse relaxation time (T_2) distribution within the pores was derived through inversion. Fluids in coal rock pores exhibit three relaxation mechanisms. When acting simultaneously, T_2 of water in the pores can be expressed as

$$\frac{1}{T_2} = \frac{1}{T_{2S}} + \frac{1}{T_{2B}} + \frac{1}{T_{2D}} = \rho\left(\frac{S}{V}\right)_p + 3\left(\frac{T_k}{298\eta}\right) + \frac{D(\gamma G T_E)^2}{12}, \quad (3)$$

where T_{2S} is the surface relaxation time of the pore fluid, T_{2B} is the bulk relaxation time of the pore fluid, T_{2D} is the T_2 relaxation time of the pore fluid caused by gradient magnetic field diffusion, ρ is the T_2 relaxation strength of the particle surface, $(S/V)_p$ is the surface-to-volume ratio of the pore, T_k is the temperature, γ is the fluid viscosity, G is the field gradient, and T_E is the echo spacing.

According to Eq. (3), T_{2B} is primarily influenced by the fluid properties, and its value is negligible compared with T_{2S}. T_{2D} is affected by G and T_E. In coal rock specimens, the values of these parameters are small, making the diffusion relaxation time negligible. Therefore,

$$\frac{1}{T_2} \approx \rho\left(\frac{S}{V}\right)_p = F_S(\rho/r), \quad (4)$$

where F_S is the pore shape parameter, where the shape parameters for the fractures, tubular pores, and spherical pores are 1, 2, and 3, respectively; r is the pore size.

Through NMR analysis, the pore structure distribution and evolutionary patterns, fluid occurrence states, and physical property-related information of coal samples soaked in mine water at varying concentrations for different soaking periods can be revealed. Figure 10 shows the T_2 spectra of coal samples soaked in highly mineralized water at a 1C standard concentration under saturated water (S_w) and irreducible water (S_{ir}) conditions after soaking periods of 0, 20, 40, 60, and 80 d. T_2 and amplitude reflect the pore size and quantity, respectively, with the pore size positively correlated with the value of T_2. The R/M symbol is defined as the sum of the porosity and other parameters for two consecutive time gradients (front/rear) under the same concentration gradient, with R indicating pre-time gradient integration (20 + 40) and M indicating post-time gradient integration (60 + 80).

During the initial soaking stage (0–40 d), the T_2 spectra distinctly reflected pore filling and wetting effects, characterized by a shift of T_2 values toward shorter relaxation times and a significant increase in the peak amplitudes of micropores and mesopores. This phenomenon indicates that under the influence of a high concentration of highly mineralized mine water, dissolution cavities are formed, leading to the interconnection of some micropores and their transformation into mesopores. As the soaking period progressed to the intermediate stage (40–80 d), the T_2 spectra revealed a widened transverse relaxation time range, continued growth in the peak amplitudes of the micropores and mesopores, and notable changes in the macropore peak amplitudes. This further confirms that over time, the number of internal pores in the coal samples increased, accompanied by a more diverse pore size distribution. This demonstrates the activation and interconnection of micropores under the hydro–mechanical–chemical coupling effects, reflecting the dynamic evolution of the originally isolated pore structures as they gradually develop, expand, and interconnect.

Finally, during the late soaking stage (80–100 d), the peak amplitudes of micropores and mesopores in the T_2 spectra stabilized, and changes in the macropore peak amplitudes were no longer significant. This indicates that the pore structure within the coal samples reached a new dynamic equilibrium state.

3.4 Computer tomography analysis of eroded coal sample and its internal structure

Three-dimensional (3D) image reconstruction based on two-dimensional images obtained from CT scanning is required to achieve quantitative 3D visualization of coal pores and fracture structures. The 3D reconstruction of the coal sample is shown in Fig. 11. Currently, several numerical analysis software tools, such as Thermo Scientific Avizo, VGStudio, MATLAB, COMSOL, and Mimics, enable the visualization and further analysis of CT grayscale images. In this study, Avizo software was used to stack and visualize the CT grayscale images in 3D. Threshold segmentation and 3D reconstruction were performed to extract a quantifiable 3D matrix structure from coal samples for quantitative analysis. The specific steps are as follows.

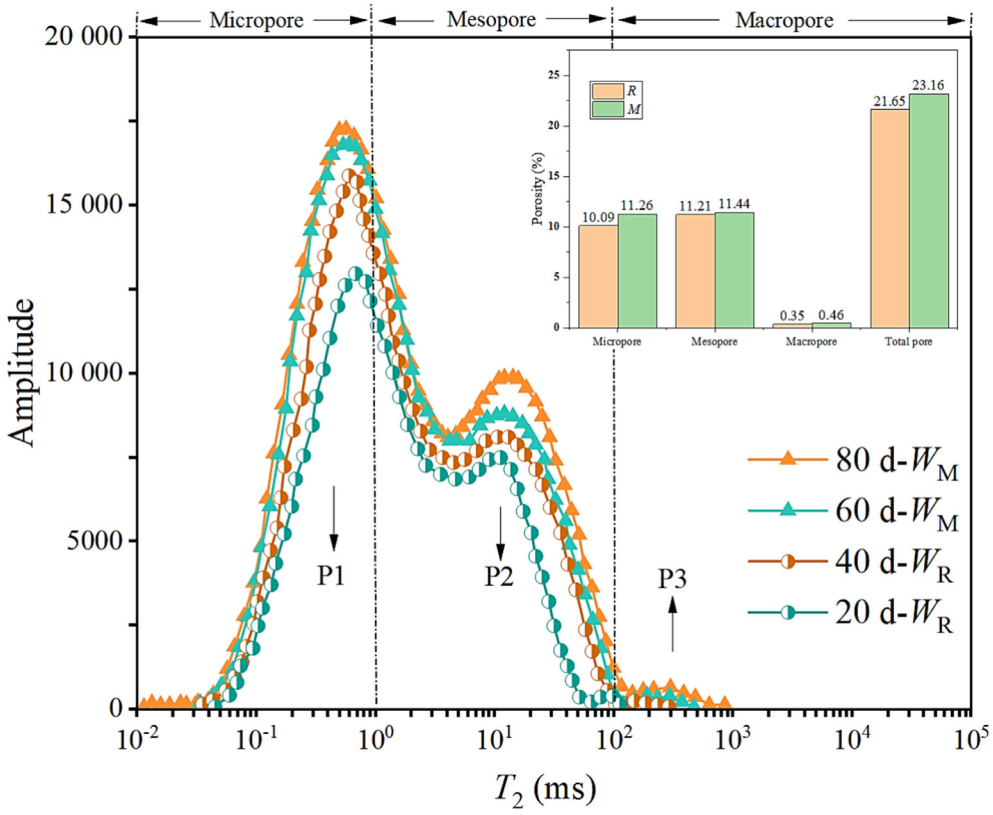

Fig. 10. T_2 spectra of coal samples immersed in highly mineralized water at 1C standard concentration for immersion periods of 0, 20, 40, 60, and 80 d.

First, a series of two-dimensional images obtained from CT scanning were imported into the 3D reconstruction software Avizo. Because of the potential noise introduced during image generation by external factors such as the rotation of the sampling stage and current fluctuations, the images may deviate from the actual condition of the coal sample. Therefore, a median filtering algorithm was applied to preprocess the images (Fig. 11(b)) to reduce the effect of random noise, enhance the image quality and accuracy, and effectively preserve the details and edge information in the images.

Next, a fast watershed algorithm, which is an improvement over the watershed algorithm based on the simulated immersion method proposed by Vincent and Soille (V–S algorithm), was employed for image segmentation. Using this method, a 3D pore model of the coal sample was obtained (Fig. 11(c) and (e)). The fast watershed algorithm demonstrated high efficiency and robustness in handling complex pore structures and effectively identified and segmented pores and fractures within the coal matrix, thereby providing a foundation for subsequent analysis.

To ensure the accuracy and reliability of the reconstructed model analysis results, the representative elementary volume (REV) was calculated. The basic approach for determining the REV size is as follows: multiple regions of interest (ROIs) of varying sizes are selected, the porosity of each ROI is calculated, and the REV size is defined as the dimension at which the porosity stabilizes. Four ROIs with different volumes were selected, ranging from 50 × 50 × 50 to 400 × 400 × 400 voxels, and incremented in steps of 50 voxels each. The REV size was determined to be 300 × 300 × 300 voxels when porosity fluctuations across the ROIs remained low. Prior to REV calculation, the original data were cropped into regularly shaped ROIs. The cubic model, which serves as a regularized reconstruction of the cylindrical sample, eliminates curvature distortion at the edges of the cylindrical specimen, enhances the comparability of statistical results, and ensures compatibility with mainstream analysis software such as Avizo.

In the image-segmentation stage, the entropy threshold algorithm was applied for preliminary extraction of the coal matrix. The advantage of this algorithm is its ability to automatically determine the optimal segmentation threshold, particularly in cases where the grey scale histogram lacks distinct valleys (a common phenomenon in which there is a significant contrast difference between the coal matrix and pores/fractures). Entropy is a quantitative measure of image information and is mathematically defined as presented in Eq. (3). The entropy threshold algorithm achieves image segmentation by identifying a threshold that minimizes the combined entropy of the background and foreground regions, thereby ensuring the scientific validity and effectiveness of the segmentation results. As shown in Fig. 11(d), the application of the

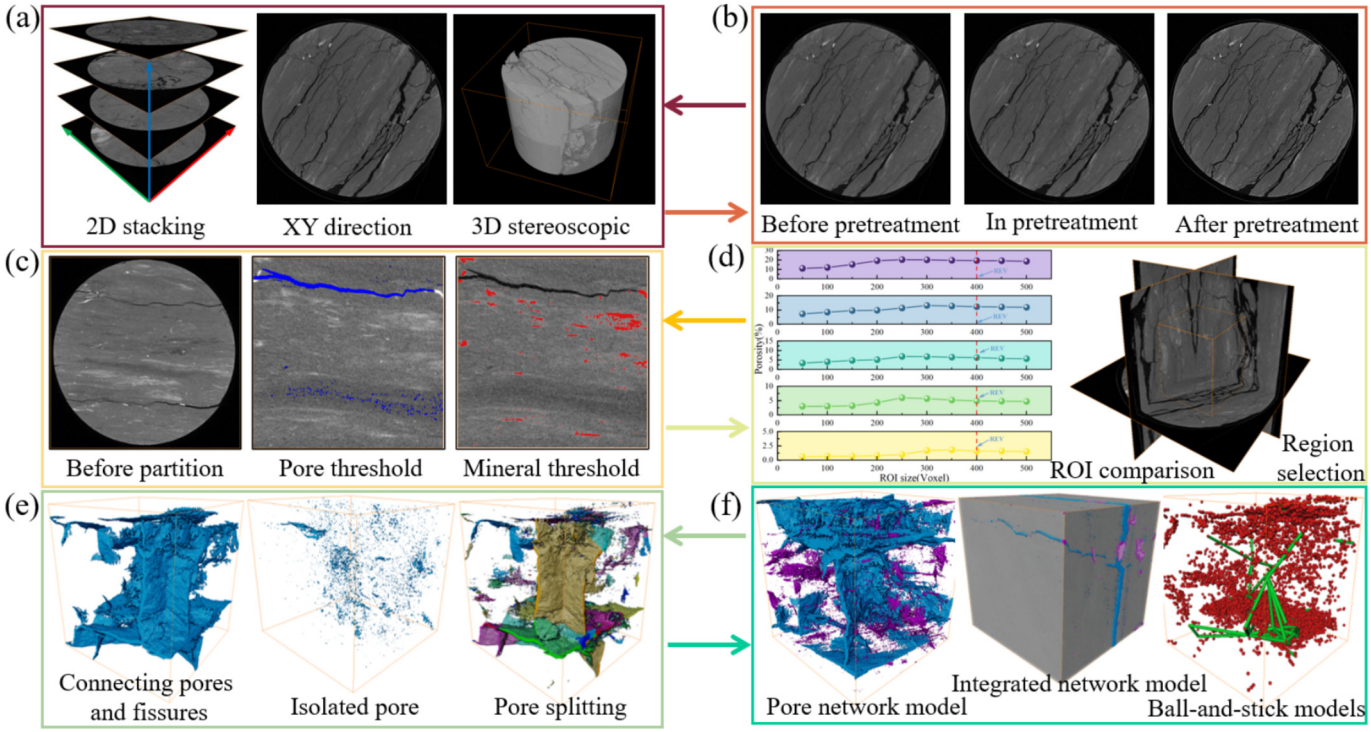

Fig. 11. Three-dimensional reconstruction process of coal sample. (a) Original CT image, (b) median filter, (c) threshold segmentation, (d) REV selection, (e) 3D reconstruction, and (f) pore network model.

entropy threshold algorithm successfully distinguished pores from the coal matrix, establishing a foundation for subsequent 3D modeling.

Figure 12 summarizes the multifaceted effects of highly mineralized mine water with varying concentration gradients on coal samples with different maturities. Through 3D visualization models, the spatial structural evolution of the coal matrix, minerals, and pores/fractures were demonstrated, and connected and nonconnected pores were clearly distinguished. These features are characterized by tonal differences (grey, purple, and blue) representing the coal matrix, minerals, and pores/fractures, respectively. The different colors in the pore network model after pore isolation represent the visual labels designed to distinguish individual pores or throat bodies.

Micromechanical analysis reveals that pore networks weaken coal rock strength through three mechanisms (Kong et al., 2024): (1) inducing localized stress concentration effects, (2) reducing effective load-bearing areas, and (3) promoting fluid–solid coupling damage. Specifically, as the immersion period increased, particularly for coal samples immersed in high-concentration aqueous solutions, the number and volume of internal pores and fractures significantly increased. Initially isolated, these pores and fractures gradually connected over time, forming an interconnected network structure. This structural transformation substantially expanded the permeable surface area, further exacerbating the physical deterioration of the coal matrix.

During the initial stages of immersion, the coal matrix exhibited high integrity. However, as the immersion period increased, particularly under the influence of medium-to-high concentrations of highly mineralized aqueous solutions, the density of the coal matrix gradually decreased, and its structural integrity significantly declined. These changes manifested as reductions in the coal matrix volume and density, accompanied by structural loosening, leading to a marked degradation of the mechanical properties of the coal samples. Additionally, with prolonged immersion time, the dissolved minerals gradually precipitated and accumulated within the pores and fractures of the coal samples. This filling phenomenon was particularly pronounced during extended immersion periods. Such mineral deposition not only alters the internal chemical environment of the coal samples, but may also redistribute internal stresses, further driving physical transformations in the matrix.

4 Discussion

4.1 Mechanism of weakly-alkaline-driven dissolution and aluminum–silicon ion release in kaolinite

The dissolution behavior of kaolinite ($Al_2Si_2O_5(OH)_4$) is highly sensitive to the solution pH. Under the given experimental conditions with pH = 7.2 (neutral to weakly alkaline), dissolution is primarily governed by OH^--dominated complexation/hydrolysis. The dominant reaction pathways were as follows:

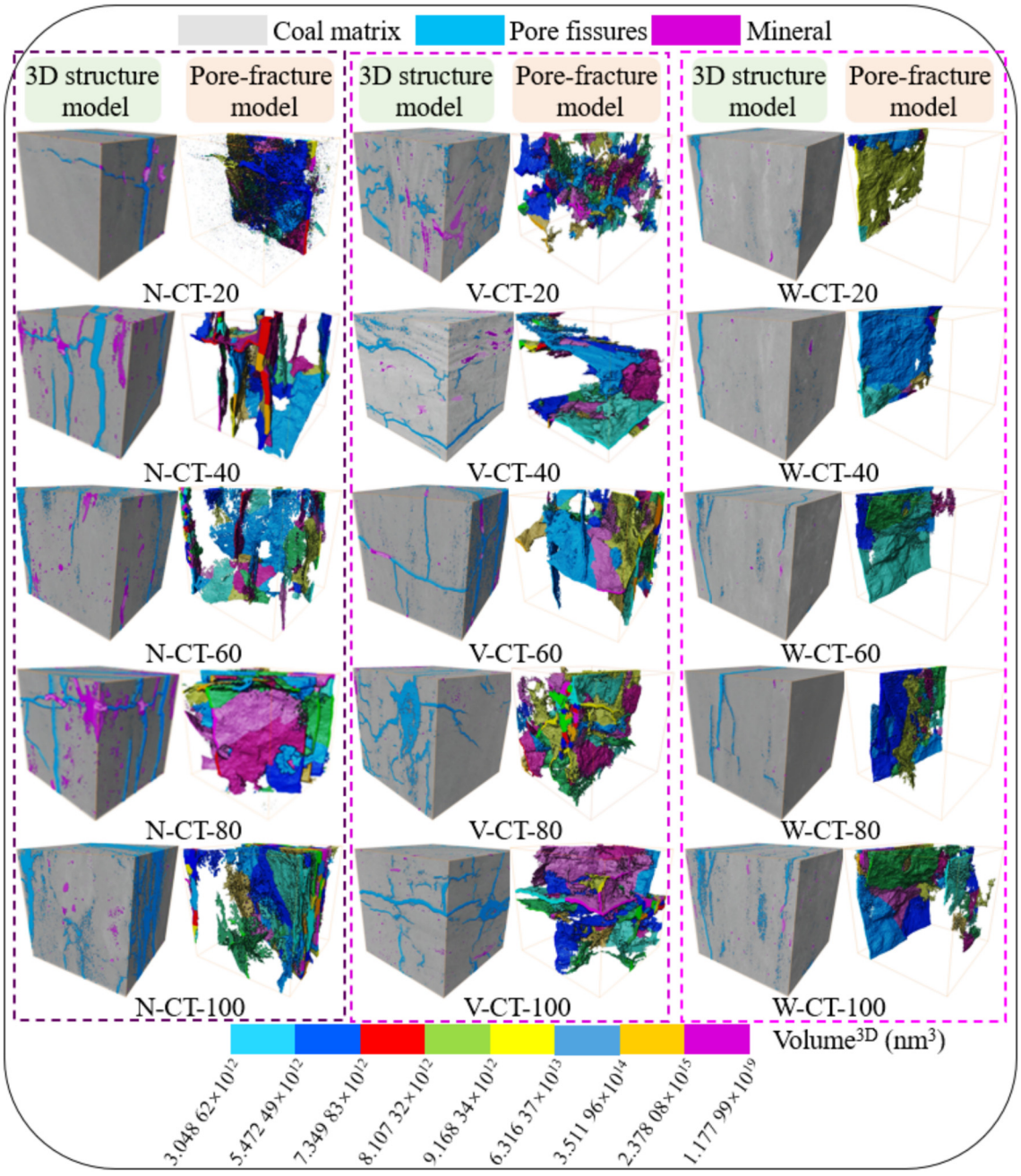

Fig. 12. Three-dimensional matrix mineral fracture structure model and pore fracture separation model.

$$Al_2Si_2O_5(OH)_4(s) + 2OH^-(aq) + 6H_2O(l) \rightarrow 2Al(OH)_4^-(aq) + 2H_4SiO_4(aq). \quad (5)$$

In OH^--bearing environments, the alumina octahedral layer of kaolinite undergoes hydrolysis, forming soluble tetrahydroxyaluminate ions, whereas silicon transforms into monomeric silicic acid. This process constitutes the primary mechanism responsible for the significant attenuation of kaolinite diffraction peak intensities in the XRD patterns.

4.2 Quartz corrosion resistance and surface passivation mechanism

Quartz exhibited exceptional chemical stability across a broad concentration range (3600–36 000 mg/L) with no significant variation in XRD peak intensities. This behavior is primarily attributed to intrinsic inertness and surface passivation mechanisms.

$$SiO_2(s, quartz) + 2H_2O(l) \rightleftharpoons H_4SiO_4(aq) \quad (6)$$

(1) Si–O tetrahedra formed a 3D network structure via high-strength Si–O covalent bonds, exhibiting a lattice energy of 12.7 kJ/cm^3. This imparts outstanding mechanical and chemical resistance.
(2) Reaction inertness manifests as substantial dissolution only under extreme conditions (>6 mol/L HF or strong bases at 200 °C).
(3) The surface silanol groups (Si–OH) underwent spontaneous dehydration condensation to generate hydrophobic siloxane bridges (Si–O–Si). This dynamic passivation layer suppresses hydrolysis corrosion rates to 1/10^5 of the dissolution rate of calcite at 25 °C.

4.3 Cascade reaction mechanism: Ion migration–differential crystallization–crystallization stress

In highly mineralized mine water (TDS > 30 000 mg/L), chloride-dominated salt precipitation constitutes the core degradation process of coal rock masses. This phenomenon fundamentally originates from ion concentrations that exceed solubility limits. Owing to its low hydration energy, Cl^- preferentially initiates salt crystallization. Sodium ions combined with chloride to form cubic halite (NaCl), as shown in Eq. (7). This crystalline phase precipitates within pore throats or on coal rock surfaces, obstructing seepage channels while exerting persistent crystallization stress on fractures through volumetric expansion.

$$Na^+(aq) + Cl^-(aq) \rightarrow NaCl(s). \quad (7)$$

The salting-out process triggers a dynamic "dissolution–migration–crystallization" cycle: NaCl crystallization directly reduces permeability (>90%); directional growth of chloride salts within fractures compresses pores, propagating microcracks; and recurrent crystallization stress generates new fractures in the rock matrix, subsequently accelerating the intrusion of Cl^--bearing fluids. This establishes a self-catalyzing destruction chain that serves as the fundamental carrier for the macroscopic mechanical degradation of coal rock masses (Fig. 13). High concentration solution (36 000 mg/L) led to the most evident decrease in yield point (29.53% decrease in uniaxial compressive strength (UCS)) and increase (9.34% increase in UCS). The longer the soaking time, the more significant the yield point decrease (22.47% decrease in UCS) and increase (7.83% increase in UCS).

4.4 Mechanism of influence of highly mineralized mine water on pore structure and crack evolution of coal rock

In this study, highly mineralized mine water solutions with different concentration gradients (36 000, 18 000, and 3600 mg/L) were used to treat anthracite coal samples for varying immersion periods. Using 3D visualization modeling techniques, the evolutionary processes of the equivalent pore network models were systematically analyzed along with their impacts on the matrix proportion, mineral proportion, pore and fracture proportions, crack density, crack length, and crack aperture, as shown in Fig. 14. The findings indicate that immersion in highly mineralized mine water solutions results in multilayered influences on the matrix, minerals, pore and fracture structures, and the related physical properties of anthracite coal samples.

The study revealed that the matrix proportion significantly decreased with prolonged immersion periods, particularly in high-concentration highly mineralized mine water solutions. This indicates that highly mineralized mine water can markedly erode anthracite coal matrices, leading to reductions in their volume and strength. During the early immersion stage (0–20 d), no significant changes were observed in the mineral proportion. However, as the immersion period increased, especially in high-concentration highly mineralized mine water solutions (up to 80 d), the mineral proportion increased substantially. These results indicate that mineral precipitation and accumulation in pores and fractures, coupled with pore and fracture expansion, collectively alter the internal chemical environment and physical properties of the coal samples.

Porosity (proportion of pores and fractures) continuously increased with prolonged immersion periods, particularly in highly mineralized mine-water solutions. When the immersion period was extended beyond 80 d, the proportion of pores and fractures significantly expanded, which was closely linked to a decline in the mechanical properties of the matrix and the deposition of minerals. 3D visualization models further revealed that with prolonged immersion periods, the crack density (specific surface area and specific volume), length, and aperture exhibited increasing trends, particularly in highly mineralized mine water environments.

Long-term immersion in highly mineralized mine water causes damage to coal rock, with microstructural changes resulting in the degradation of macroscopic mechanical behavior (Fig. 13). The key mechanisms revealed at the microscopic level are as follows:

(1) Mineral dissolution and structural instability: XRD analysis revealed that the dynamic chemical erosion dominated by Cl^-, characterized by "dissolution–migration–crystallization", significantly dissolved clay minerals (such as kaolinite) and induced interlayer expansion disintegration. Mineral dissolution directly weakened the cementation strength between the particles. The SEM observation (Fig. 9(a)) clearly shows the formation of initial microcracks or spalling layers caused by cement rupture and confirms the intensification of fragmentation.
(2) Pore-fracture network evolution: CT analysis indicated that the synergistic action of mineral dissolution-induced pore enlargement and new fracture formation led to a 10.7% decrease in the coal

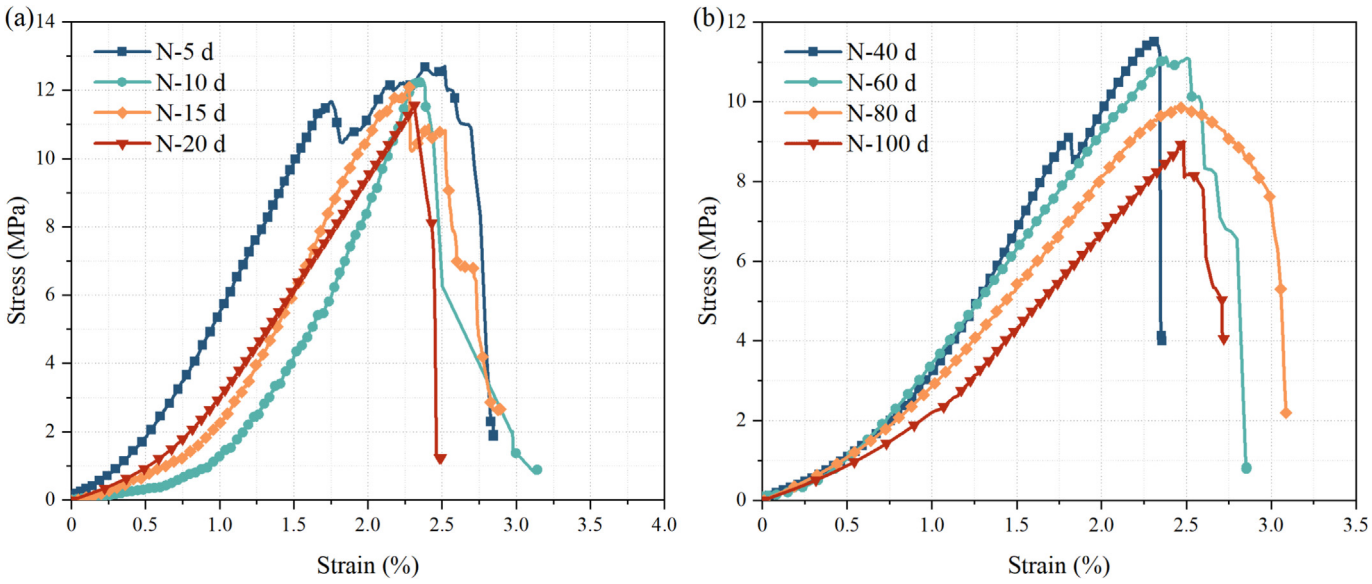

Fig. 13. Uniaxial compression stress–strain curves of coal rock at different soaking ages. (a) N5–N20 d groups, and (b) N40–N100 d groups.

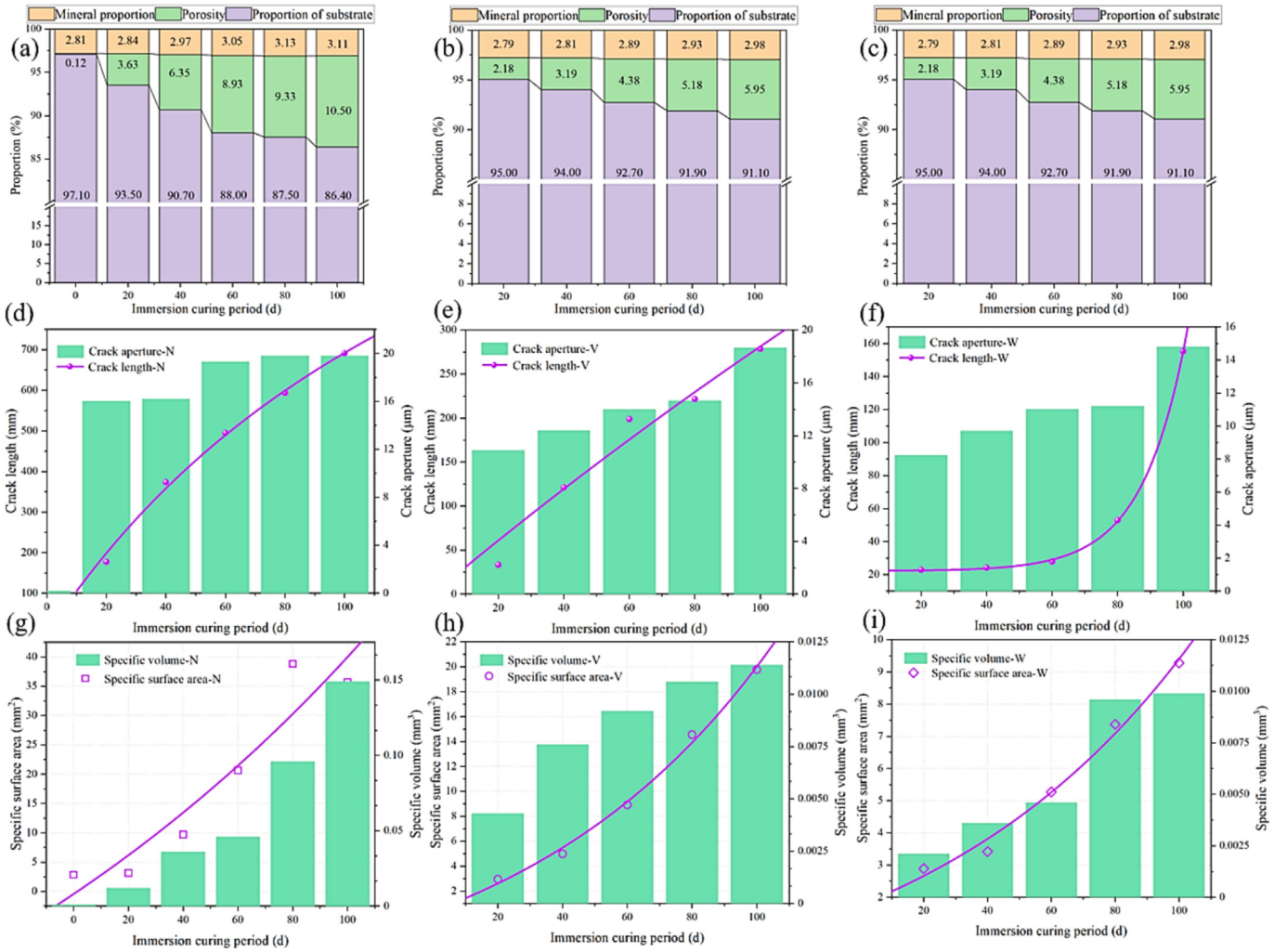

Fig. 14. Two-dimensional and three-dimensional matrix, mineral, and fracture spatial distribution in N-CT-100 sample.

matrix volume proportion and a significant 10.38% increase in porosity. Notably, the fracture connectivity transitioned from an "isolated" state to an "interconnected network".

The simultaneous degradation of macroscopic mechanical behavior is manifested as

(1) Attenuation of strength and deformation characteristics: UCS showed a significant reduction of 29.53%, and the yield point advancement rate reached 9.34%.
(2) Fracture network pattern evolution: The failure of pristine coal rock is governed by a single dominant shear fracture. After long-term immersion in a highly mineralized solution, CT 3D reconstruction revealed that the fracture network transitions from single-path penetration to multi-directional networked development, forming a fracture network pattern dominated by branched and interconnected composite fractures.

This coupled micro–macro degradation process reveals the existence of a nonlinear positive feedback mechanism between sustained mineral dissolution and accelerated fracture network connectivity. Ultimately, as shown in the stress–strain curve of the high-concentration group in Fig. 13, this mechanism causes a leftward shift in the peak stress and an intensified post-peak stress drop, presenting a typical brittle-to-ductile transition (or brittle-to-ductile conversion) and confirming the significance of the chemo-mechanical coupling effect.

5 Conclusions

This study focused on coal pillar dams in underground reservoirs of highly mineralized mine water storage in the Lingxin Coal Mine. Highly mineralized mine water erosion, XRD, SEM, and NMR tests, as well as CT microstructure observations of the coal samples were conducted. These investigations revealed the damage and deterioration mechanisms of highly mineralized mine water erosion on the microstructural characteristics of coal pillar dams. The main conclusions of this study are as follows:

(1) Highly mineralized mine water markedly deteriorates the mineral composition and crystal structure of coal rock. In a weakly alkaline environment, the OH^--driven hydrolysis of the octahedral aluminum–oxygen layer in kaolinite leads to a significant attenuation in the XRD peak intensity. Quartz exhibits chemical inertness owing to its 3D network of Si–O bonds and the formation of a self-healing passivation layer resulting from the dehydration and condensation of the surface silanol groups. In the coal samples, the interlayer d-spacing (d_{002}) increased and the aromaticity degree (f_a) decreased. A high-concentration environment (36 000 mg/L) induced significant crystal lattice modification.
(2) The microstructural damage induced by highly mineralized mine water erosion evolved progressively in three stages. In the initial stage, mineral dissolution triggered structural loosening at the boundaries, forming the initial pathways. In the mid-stage, the delamination of layered minerals extended into deeper zones, accelerating the development of pore networks, as manifested by broadening of the T_2 spectra and continuous increases in micropore/mesopore peak amplitudes. In the later stages, organic matter migration and dissolution-induced voids led to irreversible structural damage, with chloride deposits accumulating on the surfaces. CT observations confirmed that as the soaking duration increased, isolated pores transformed into connected networks, and the enlarged percolation area exacerbated matrix deterioration.
(3) Chloride ions (Cl^-) acted as the core driving factor. Owing to their low hydration energy, Cl^- preferentially combined with sodium ions (Na^+), crystallizing as halite in supersaturated solutions. Crystallization within the pore throats generated two effects: seepage obstruction and salt-expansion stress induction through volumetric expansion. Salt-expansion stress compressed pore walls, triggering the propagation of microcracks. Newly formed channels accelerated the intrusion of Cl^--bearing solutions, establishing a cyclic "dissolution–migration–crystallization–crack propagation" process.
(4) In the long-term sealed environment of highly mineralized mine water, the dynamic erosion dominated by Cl^- through mineral dissolution–migration–crystalli zation triggered microstructural damage to coal rock (including dissolution and disintegration of clay minerals, cementation fracture, 10.38% increase in porosity, and fracture network interconnection). This resulted in the nonlinear degradation of macroscopic mechanical behavior, manifested as a 29.53% reduction in UCS, 9.34% increase in the yield point, and a fracture network pattern transitioning from single-path penetration to multidirectional networked development.

Data availability

The data that support the findings of this study are available from the corresponding author upon reasonable request.

CRediT authorship contribution statement

Hao Liu: Formal analysis, Data curation, Conceptualization. **Zenghui Zhao:** Project administration, Methodology. **Qing Ma:** Investigation. **Xiaoli Liu:** Validation, Supervision. **Longjie Zhu:** Software.

Declaration of competing interest

The authors declare that they have no known competing financial interests or personal relationships that could have appeared to influence the work reported in this paper.

Acknowledgement

This work is supported by the Shandong Provincial Natural Science Foundation (Grant No. ZR2023ME086), the National Natural Science Foundation of China (Grant No. 52304093), and China Postdoctoral Science Foundation (Grant No. 2023M741968).

References

Ai, T., Wu, S. Y., Zhang, R., Gao, M. Z., Zhou, J. F., Xie, J., Ren, L., & Zhang, Z. P. (2021). Changes in the structure and mechanical properties of a typical coal induced by water immersion. *International Journal of Rock Mechanics and Mining Sciences*, *138*(9), 104597.

Berrezueta, E., Kovacs, T., Herrera-Franco, G., Mora-Frank, C., Caicedo-Potosí, J., Carrión-Mero, P., & Carneiro, J. (2023). Laboratory studies on CO_2-brine-rock interaction: An analysis of research trends and current knowledge. *International Journal of Greenhouse Gas Control*, *123*, 103842.

Chen, B. Q., Liu, H., Li, Z. H., Zheng, M. N., Yu, Y., Yu, H., Qin, L., Yang, J. L., & Yang, Y. (2023). Research progress and prospect of secondary subsidence monitoring, prediction and stability evaluation in closed underground mines. *Journal of China Coal Society*, *48*(2), 943–958 (in Chinese).

Chen, H. H., Ramandi, H. L., Craig, P., Crosky, A., & Saydam, S. (2022). Stress corrosion cracking of cable bolts in tunnels: An in-situ testing approach. *Tunnelling and Underground Space Technology*, *123*, 104421.

Chu, H. Q., Huang, Z., Zhang, Z. K., Yan, X. Y., Qiu, B. B., & Xu, N. (2024). Integration of carbon emission reduction policies and technologies: Research progress on carbon capture, utilization and storage technologies. *Separation and Purification Technology*, *343*, 127153.

Craig, P., Ramandi, H. L., Chen, H. H., Vandermaat, D., Crosky, A., Hagan, P., Hebblewhite, B., & Saydam, S. (2021). Stress corrosion cracking of rockbolts: An in-situ testing approach. *Construction and Building Materials*, *269*, 121275.

Cui, J., Jiang, Q., Li, S. J., Feng, X. T., Zhang, Y. L., & Shi, Y. E. (2020). Numerical study of anisotropic weakening mechanism and degree of non-persistent open joint set on rock strength with particle flow code. *KSCE Journal of Civil Engineering*, *24*(3), 988–1009.

Dai, L. P., Feng, D. J., Pan, Y. S., Wang, A. W., Ma, Y., Xiao, Y. H., & Zhang, J. Z. (2025). Quantitative principles of dynamic interaction between rock support and surrounding rock in rockburst roadways. *International Journal of Mining Science and Technology*, *35*(1), 41–55.

Fang, M. Y., Li, X. Y., Zhang, G., Liu, Q., Tuo, K. Y., & Liu, S. Q. (2022). Research on water-rock interaction mechanism in coal mine underground reservoir-taking Daliuta Coal Mine as an example. *Journal of China Coal Society*, *50*(11), 236–242 (in Chinese).

Fang, Y., Zhou, B., Zhang, R. Y., Wang, Y. B., Dou, L. P., & Yao, Y. X. (2024). Soil conditioning of clay based on interface adhesion mechanism: Microscopic simulation and laboratory experiment. *Underground Space*, *18*, 239–255.

Gu, D. Z. (2015). Theory framework and technological system of coal mine underground reservoir. *Journal of China Coal Society*, *40*(2), 239–246 (in Chinese).

He, Y., Li, Y. Z., Pan, Y., Shang, J. Y., Sun, W. M., Wang, M., Fan, H., Sanford, R. A., Wei, N., Peng, S. M., Xie, D. H., Zhang, W. G., Chen, S. L., Liu, Y., Jiang, Z., Jiang, Y. G., Hu, Y. D., Li, S. Y., Hu, N., Dong, Y. R., & Shi, L. (2024). Intimate microbe-water-mineral interactions mediate alkalization in the pyroxene-rich iron ore mines in Panxi area, Southwest China. *Journal of Hazardous Materials*, *480*, 136127.

Huang, S. L., Zhang, J. X., Ding, X. L., Zhang, C. Q., Han, G., Yu, G. Q., & Qu, L. L. (2024). Investigation of anisotropic strength criteria for layered rock mass. *Journal of Rock Mechanics and Geotechnical Engineering*, *16*(4), 1289–1304.

Khimulia, V., Karev, V., Kovalenko, Y., & Barkov, S. (2024). Changes in filtration and capacitance properties of highly porous reservoir in underground gas storage: CT-based and geomechanical modeling. *Journal of Rock Mechanics and Geotechnical Engineering*, *16*(8), 2982–2995.

Kong, L., Shang, J. L., Ranjith, P. G., Li, B. Q., Song, Y. Q., Cai, W. Q., & Ling, F. L. (2024). Grain-based DEM modelling of mechanical and coupled hydro-mechanical behaviour of crystalline rocks. *Engineering Geology*, *339*, 107649.

Li, G., Tang, C. N., & Liang, Z. Z. (2017). Development of a parallel FE simulator for modeling the whole trans-scale failure process of rock from meso- to engineering-scale. *Computers & Geosciences*, *98*, 73–86.

Li, T. B., Chen, C., Peng, F., Ma, C. C., Li, M., & Wang, Y. X. (2024). Creep damage constitutive model of rock based on the mechanisms of crack-initiated damage and extended damage. *Underground Space*, *18*, 295–313.

Pan, Y. S., & Wang, A. W. (2023). Disturbance response instability theory of rock bursts in coal mines and its application. *Geohazard Mechanics*, *1*(1), 1–17.

Pazki, S., Benboudjema, F., Bourdot, A., Langlois, S., Fau, A., Hafid, F., & Honorio, T. (2025). Crystallization pressure in ASR expansion quantified by thermodynamic modeling and micromechanics. *Cement and Concrete Research*, *193*, 107878.

Saberi, N., & Vriens, B. (2025). Compositional heterogeneity of secondary minerals in mine waste rock: Origins and implications for water quality. *Journal of Hazardous Materials*, *487*, 137163.

Shen, R. X., Li, H. R., Wang, E. Y., Chen, T. Q., Li, T. X., Tian, H., & Hou, Z. H. (2020). Infrared radiation characteristics and fracture precursor information extraction of loaded sandstone samples with varying moisture contents. *International Journal of Rock Mechanics and Mining Sciences*, *130*, 104344.

Tang, X. H., Xu, J. J., Zhang, Y. H., Zhao, H. F., Paluszny, A., Wan, X., & Wang, Z. Z. (2023). The rock-forming minerals and macroscale mechanical properties of asteroid rocks. *Engineering Geology*, *321*, 107154.

Wu, S. S., Hao, W. Q., Yao, Y., & Li, D. Q. (2023). Investigation into durability degradation and fracture of cable bolts through laboratorial tests and hydrogeochemical modelling in underground conditions. *Tunnelling and Underground Space Technology*, *138*, 105198.

Xie, H. P., Gao, M. Z., Liu, J. Z., Zhou, H. W., Zhang, R. X., Chen, P. P., Liu, Z. Q., & Zhang, A. L. (2018). Research on exploitation and volume estimation of underground space in coal mines. *Journal of China Coal Society*, *43*(6), 1487–1503 (in Chinese).

Xu, H. C., Lai, X. P., Shan, P. F., Yang, Y. B., Zhang, S., Yan, B. X., Zhang, Y., & Zhang, N. (2023). Energy dissimilation characteristics and shock mechanism of coal-rock mass induced in steeply-inclined mining: Comparison based on physical simulation and numerical calculation. *Acta Geotechnica*, *18*, 843–864.

Xu, Q., Li, P. F., Xu, C. B., Wang, S. Q., & Zhang, S. L. (2025). Investigation of the spatial distribution of tunnel seepage under varying drainage capacities in water-abundant regions. *Underground Space*, *23*, 343–361.

Zeng, L., Yu, H. C., Qiu, J., Luo, J. T., Liu, J., Gao, Q. F., & Zhang, H. R. (2024). Pore characteristics and microscopic damage mechanism of disintegrated carbonaceous mudstone exposed to dry-wet cycles. *Construction and Building Materials*, *433*, 136774.

Zhang, C., Wang, F. T., & Bai, Q. S. (2021). Underground space utilization of coalmines in China: A review of underground water reservoir construction. *Tunnelling and Underground Space Technology*, *107*, 103657.

Zhang, Y. L., Ma, G. W., & Li, X. D. (2024a). Mode-I fracture toughness and damage mechanism of dry and saturated sandstone subject to cryogenic condition. *International Journal of Rock Mechanics and Mining Sciences*, *180*, 105796.

Zhang, Y. L., Gu, Y. M., & Ma, G. W. (2024b). Mode-I fracture toughness and fracturing damage model for sandstone subjected to cryogenic treatment to –160 °C. *Rock Mechanics and Rock Engineering*, *57*(10), 7929–7943.

Zhang, Y. J., Cao, Z., Liu, C., & Huang, H. W. (2024c). Fluid-solid coupling numerical simulation of micro-disturbance grouting treatment for excessive deformation of shield tunnel. *Underground Space*, *19*, 87–100.

Zhao, Y. B., Chen, T. L., & Wang, J. (2025). Size-dependent airborne metal solubility and associated analytical techniques at bulk and single particle levels: A review. *Atmospheric Environment*, *358*, 121343.

Zhao, Z. H., Liu, H., Ma, Q., & Shuang, J. L. (2023). Micro-macro damage, deterioration and cracking of heterogeneous composite rock masses with non-penetrating cracks under uniaxial compression. *Theoretical and Applied Fracture Mechanics*, *125*, 103919.

Zhou, L. M., Zhu, Z. D., Oterkus, E., Oterkus, S., & Xu, H. C. (2023). Research on the effects of heating and cooling processes on the mechanical properties of yellow rust granite. *Geohazard Mechanics*, *1* (3), 231–243.